Supporting Information

Solvothermally optimizing Ag_2Te/Ag_2S composites with high thermoelectric performance and plasticity

Min Zhu,[1,a] Xiao-Lei Shi,[2,a] Meng Li,[2] Hao Wu,[1] De-Zhuang Wang,[1] Liang-Cao Yin,[1] Ting Wu,[1] Wei-Di Liu,[2] Yan Huang,[1] Zhi-Gang Chen [2,]* and *Qingfeng Liu[1,*]*

[1] State Key Laboratory of Materials-Oriented Chemical Engineering, College of Chemical Engineering, Nanjing Tech University, Nanjing 211816, China.

[2] School of Chemistry and Physics and Center for Materials Science, Queensland University of Technology, Brisbane, Queensland 4000, Australia.

[a] These authors contribute equally to this work.

[*] E-mail: zhigang.chen@qut.edu.au (ZGC); qfliu@njtech.edu.cn (QL).

Section 1. Experimental details.

Chemicals: The raw materials include silver chloride (AgCl, 99.5%, Aladdin), sodium tellurite (Na_2TeO_3, 97%, Aladdin), sodium sulfide nonahydrate ($Na_2S·9H_2O$, 98%, Macklin), sodium hydroxide (NaOH, Macklin), and ethylene glycol (99%, Shanghai Lingfeng Chemical Reagent Co. Ltd.).

Solvothermal synthesis: In this work, we prepared three samples with different ratios: $Ag_2Te_{0.1}S_{0.9}$, $Ag_2Te_{0.2}S_{0.8}$, and $Ag_2Te_{0.3}S_{0.7}$. In our synthesis method, 2 g of NaOH was dissolved in 5 ml of deionized water, and 45 ml of ethylene glycol was subsequently added. The components were proportioned according to the molar ratio. The three samples were loaded into the kettle for reaction at 230 °C for 12 hours. The products were washed repeatedly with ethanol and deionized water, then dried in a vacuum oven at 70 °C for 12 hours. Finally, the samples were sintered using spark plasma sintering (SPS, LABOX-110H Sinter Land) under a pressure of 40 MPa at 513 K for 5 minutes.

Characterizations: The qualitative analysis of the materials was performed using X-ray diffraction (XRD, Smartlab 3 KW, with Cu source). The phase composition of the materials was analyzed using tabletop optical microscopy (Hitachi TM3000) combined with X-ray energy-dispersive spectroscopy (EDS, OXFORD Xplore). The cross-sectional morphology of the bulk materials was examined using field emission scanning electron microscopy (S4800-Hitachi). Microstructural images were obtained using transmission electron microscopy (TEM, Hitachi HF5000 Cs-STEM/TEM).

Thermoelectric property measurement: We used the instrument (SBA 458, NETZSCH, Germany) to measure the electrical conductivity (σ) and Seebeck coefficient (S). The thermal conductivity (κ) was calculated using the formula $\kappa = D \times C_p \times \rho$, where D is the thermal diffusivity, C_p is the specific heat capacity, and ρ is the density. The D was measured with the instrument LFA 457 (NETZSCH, Germany). The C_p of Samples 1-3 was measured using a Differential Scanning Calorimeter (DSC) (TA Q-20, USA). The C_p of intrinsic Ag_2Te was calculated using the Dulong-Petit law. The electronic

thermal conductivity (κ_e) was calculated using the formula $\kappa_e = L\sigma T$, where L is the Lorenz number. The Hall coefficient (R) was measured by the Van der Pauw method (CH-70, CH-Magnetoelectricity Technology Co., Ltd., China). The carrier concentration (n) and mobility (μ) were determined using the equations $n = 1/eR$ and $\mu = \sigma R$, respectively. The bending performance was tested using an INSTRON 5982 with a loading rate of 0.5 mm min^{-1}.

First-principles calculations: First-principle calculations were performed based on density-functional theory (DFT) with all electron projected augmented wave (PAW) method, as implemented in the Vienna Ab initio Simulation Package (VASP) [1-6]. Semi-local generalized gradient approximation (GGA) with the fully relativistic Perdew-Burke-Ernzerhof (PBE) exchange correlation functional was employed [7]. The valence wave functions were expanded in a plan-wave basis with a cut-off energy of 450 eV. The first Brillouin zone was sampled by a Monkhorst-Pack **k**-mesh of 0.18 per Angstrom for ionic relaxation and 0.12 per Angstrom for self-consistency. All atoms were allowed to relax in their geometric optimizations until the Hellmann–Feynman force is less than 1×10^{-3} eV·Å^{-1}, and the convergence criterion for the electronic self-consistent loop was set to 1×10^{-7} eV. To avoid underestimation of bandgap, the modified Becke–Johnson (mBJ) method was used for calculating electron band structures along the line-mode **k**-path based on Brillouin path features indicated by the AFLOW framework [8, 9].

Modelling: The details of the single parabolic band (SPB) modeling are:

$$S(\eta) = \frac{k_B}{e}\cdot\left[\frac{\left(g+\frac{5}{2}\right)\cdot F_{g+\frac{3}{2}(\eta)}}{\left(g+\frac{3}{2}\right)\cdot F_{g+\frac{1}{2}(\eta)}} - \eta\right] \quad \text{(S1)}$$

$$n = \frac{1}{e \cdot R_H} = \frac{(2m^* \cdot k_B T)^{\frac{3}{2}}}{3\pi^2 \hbar^3} \cdot \frac{(g + \frac{3}{2})^2 \cdot F_{g+\frac{1}{2}}^{2}(\eta)}{\left(2g + \frac{3}{2}\right) \cdot F_{2g+\frac{1}{2}}(\eta)} \tag{S2}$$

$$\mu = \left[\frac{e\pi\hbar^4}{\sqrt{2}(k_B T)^{\frac{3}{2}} E_{def}^{\ 2} (m^*)^{\frac{5}{2}}} \frac{C_l}{}\right] \frac{\left(2g + \frac{3}{2}\right) \cdot F_{2g+\frac{1}{2}}(\eta)}{(g + \frac{3}{2})^2 \cdot F_{g+\frac{1}{2}}(\eta)} \tag{S3}$$

$$L = \left(\frac{k_B}{e}\right)^2 \cdot \left\{\frac{\left(g + \frac{7}{2}\right) \cdot F_{g+\frac{5}{2}}(\eta)}{\left(g + \frac{3}{2}\right) \cdot F_{g+\frac{1}{2}}^{(\eta)}} - \left[\frac{\left(g + \frac{5}{2}\right) \cdot F_{g+\frac{3}{2}}^{(\eta)}}{\left(g + \frac{3}{2}\right) \cdot F_{g+\frac{1}{2}}(\eta)}\right]^2\right\} \tag{S4}$$

where η is the reduced Fermi level, k_B is the Boltzmann constant, g is the carrier scattering factor (g = –1/2 for acoustic phonon scattering), m^* is the effective mass, $\hbar$ is the reduced plank constant, C_l is the elastic constant for longitudinal vibrations, E_{def} is the deformation potential coefficient, and L is the Lorenz number. Moreover,

$$C_l = v_l^2 \cdot \rho \tag{S5}$$

where v_l is the longitudinal sound velocity of ~3150 m s^{-1} [10]. $F_i(\eta)$ is the Fermi integral, expressed as [11-14]:

$$F_i(\eta) = \int_0^\infty \frac{x^i}{1 + e^{(x-\eta)}} dx \tag{S6}$$

Section 2. Supporting figures.

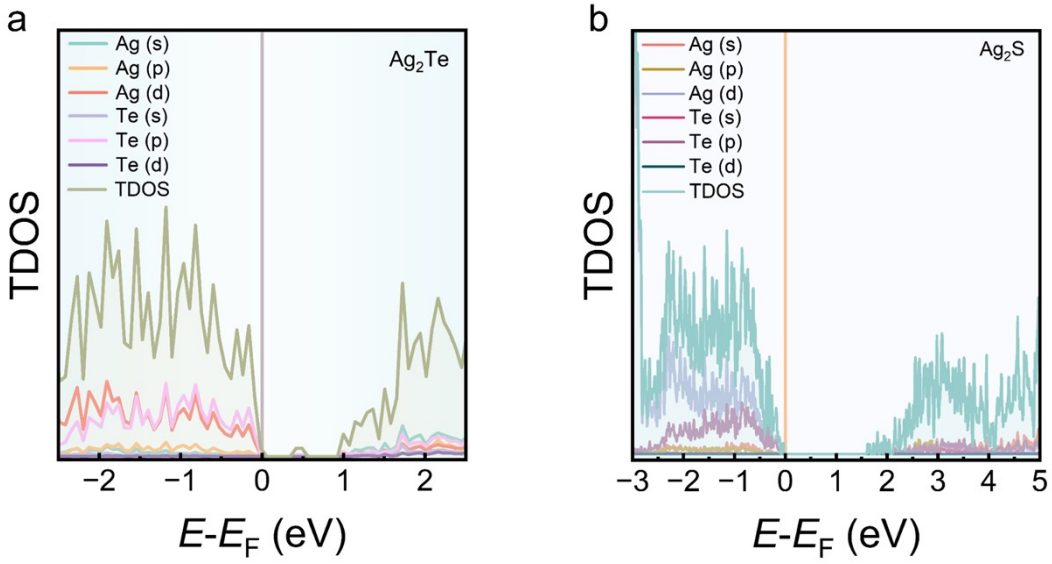

Fig. S1. Total and partial density of state (TDOS and PDOS) of (**a**) Ag_2Te and (**b**) Ag_2S.

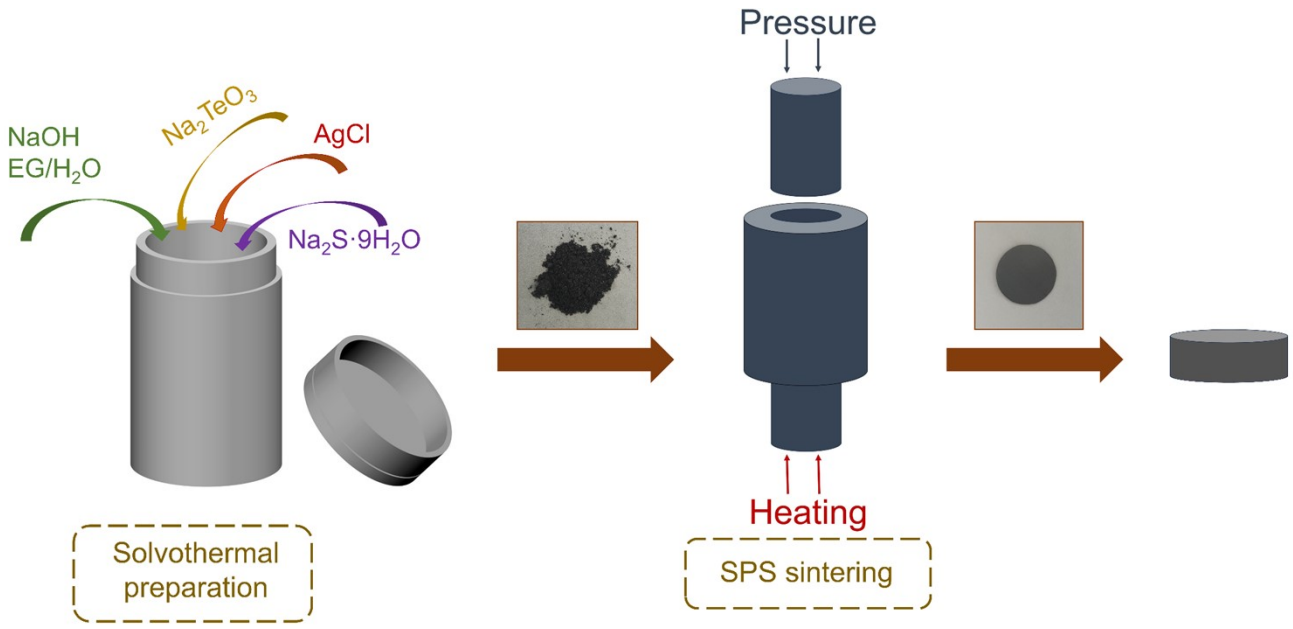

Fig. S2. Schematic diagram of the sample preparation process.

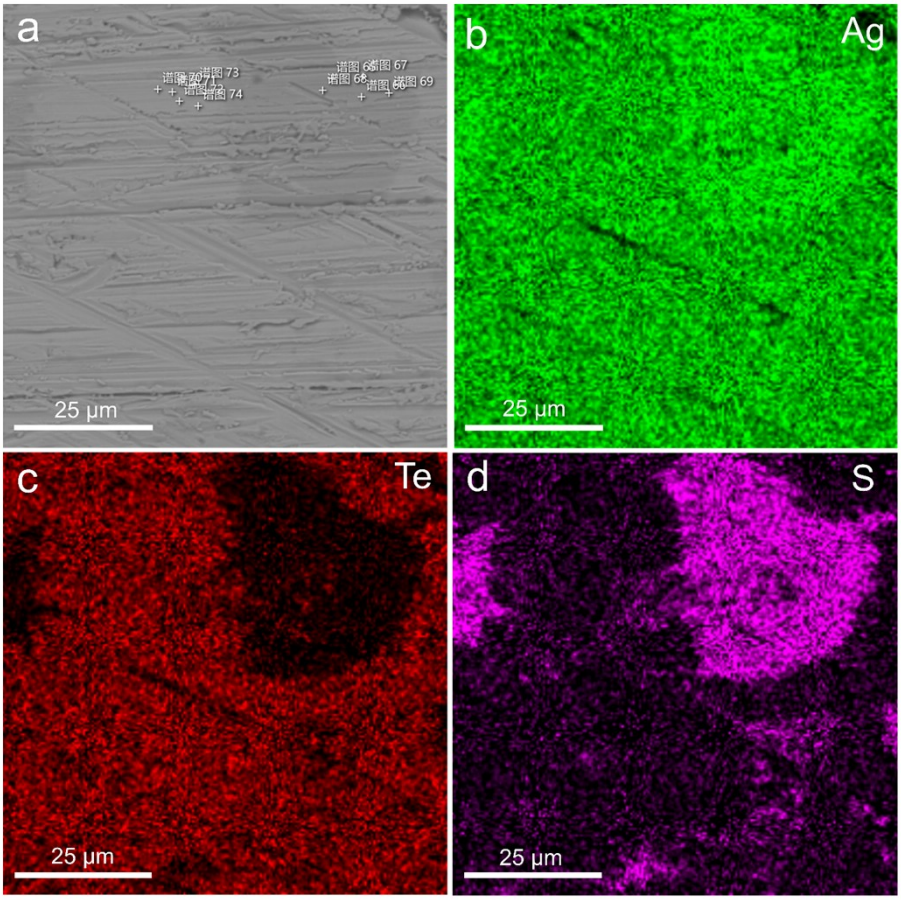

Fig. S3. (**a**) Scanning electronic microscopy (SEM) image of $Ag_2Te_{0.2}S_{0.8}$ and energy-dispersive spectroscopy (EDS) maps of individual (**b**) Ag, (**c**) Te, and (**d**) S elements.

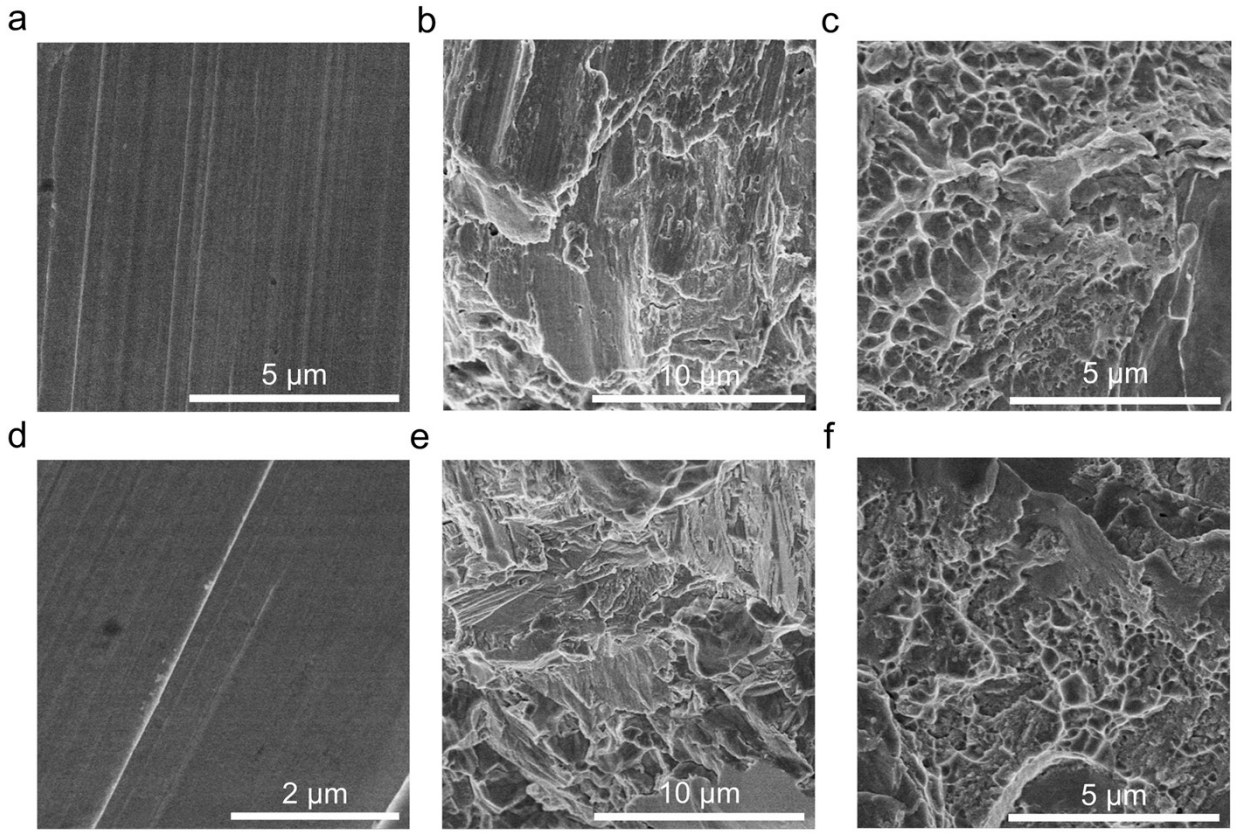

Fig. S4. SEM images of (**a**) polished and (**b-c**) fractured surfaces of $Ag_2Te_{0.1}S_{0.9}$ and (**d**) polished and (**e-f**) fractured surfaces of $Ag_2Te_{0.3}S_{0.7}$.

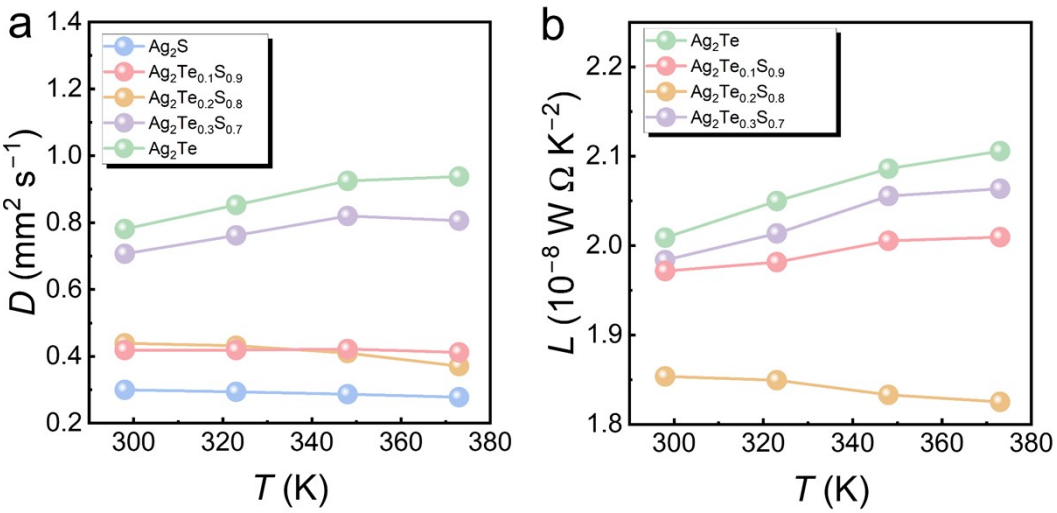

Fig. S5. Temperature-dependent thermal transport properties of $Ag_2Te_xS_{1-x}$. (**a**) thermal diffusivity (D) and (**b**) Lorenz number (L).

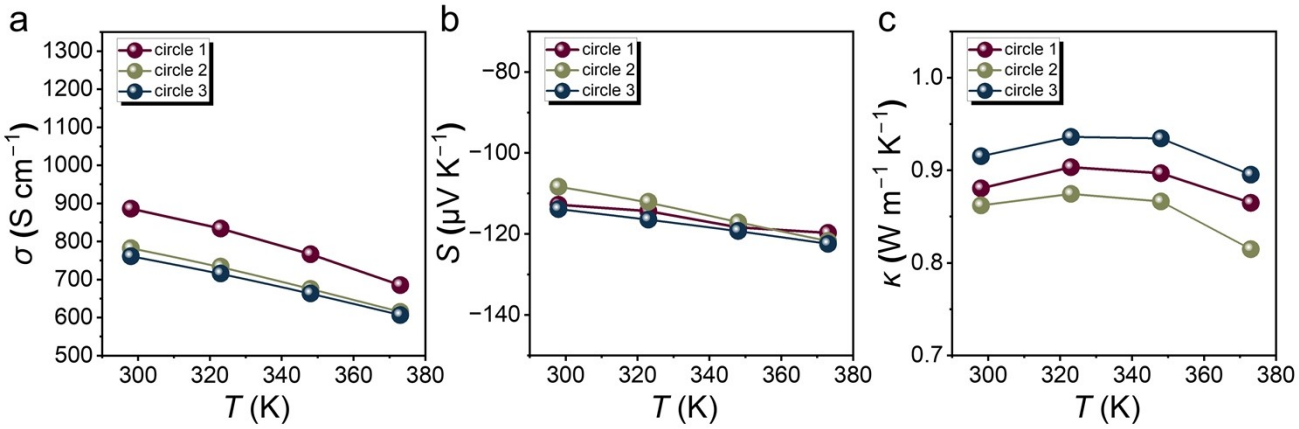

Fig. S6. The thermoelectric properties for $Ag_2Te_{0.2}S_{0.8}$ after three thermal cycle tests. **(a)** electrical conductivity (σ) **(b)** Seebeck coefficient (S) and **(c)** thermal conduction (κ).

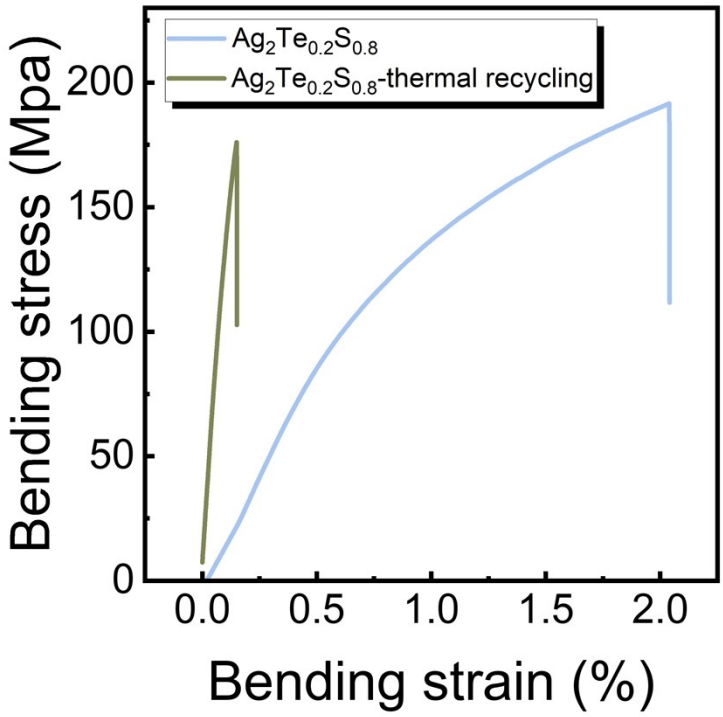

Fig. S7. Comparison of bending strain before and after thermal cycling of $Ag_2Te_{0.2}S_{0.8}$.

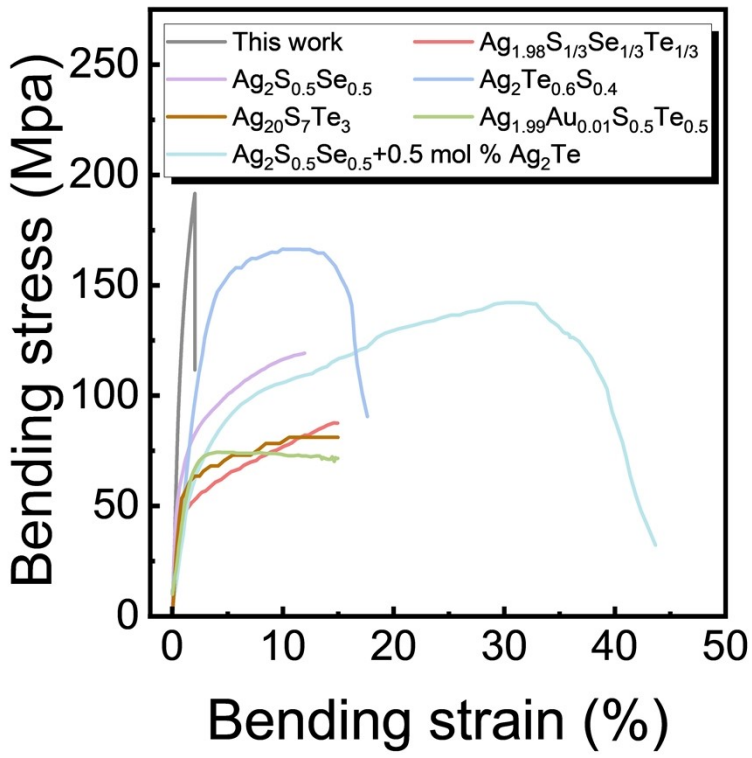

Fig. S8. Bending strain of $Ag_2Te_{0.2}S_{0.8}$ versus other Ag_2S-based thermoelectric materials [15-20].

Section 3. Supporting tables.

Table S1. A summary of thermoelectric properties of n-type Ag_2Te-based thermoelectric materials.

Preparation method	***T*** **(K)**	***σ*** **(cm^{-1})**	***S*** **(μV K^{-1})**	***S*^{2}*σ*** **(μW cm^{-1} K^{-2})**	***κ*** **(W m^{-1} K^{-1})**	***ZT***	**Ref**
Solvothermal +SPS	373	685	–119	9.83	0.86	0.42	This work
Melting	300	661	–88	5.1	0.93	0.17	[21]
Solution method	300	400	–120	5.76	0.82	0.21	[22]
Solvothermal	300	819.9	–72	4.25	0.53	0.23	[23]
Melting	375	240	–152	5.5	0.58	0.35	[24]
One-pot hydrothermal	313	245	–135.5	4.5	0.29	0.48	[25]
Melting	600	443	–128	7.25	0.74	0.6	[26]
Melting	380	910	–123	13.7	0.9	0.61	[27]
Melting	573	510	–120	7.34	0.65	0.7	[20]
One-step hot-pressing	550	240	–158	6	0.46	0.72	[28]
Melting + SPS	570	187	–187	6.5	0.49	0.72	[29]
Melting	573	372	–139	7.2	0.52	0.8	[30]
Solution method	480	363	–176	11.25	0.63	0.86	[31]
Solvothermal +SPS	633	424	–135	7.7	0.49	1.1	[32]
Hydrothermal	373	1973	–100	19.7	0.53	1.37	[33]
Melting	410	885	–106	9.9	0.3	1.4	[34]

Table S2. A summary of thermoelectric properties of n-type Ag_2S-based thermoelectric materials.

Preparation method	***T*** **(K)**	***σ*** **(cm^{-1})**	***S*** **(μV K^{-1})**	***S*^{2}*σ*** **(μW cm^{-1} K^{-2})**	***κ*** **(W m^{-1} K^{-1})**	***ZT***	**Ref**
Solvothermal +SPS	373	685	–119	9.83	0.86	0.42	This work
Melting + SPS	450	682	–70	3.34	0.85	0.2	[35]
Melting + SPS	300	360	–119	5.2	0.65	0.24	[36]
Melting	343	513	–98	5	0.4	0.42	[37]
Melting + SPS	323	332	–132	5.78	0.44	0.43	[16]
Melting	300	270	–136	4.96	0.33	0.44	[18]
Melting + Grinding + SPS	310	660	–96	6.1	0.4	0.47	[38]
Melting + SPS	723	461	–117	6.3	0.77	0.59	[39]
Melting	450	234	–150	5.3	0.44	0.63	[18]
Melting	470	230	–173	6.8	0.47	0.68	[40]
Melting	573	510	–120	7.34	0.65	0.7	[20]
Melting	460	180	–187	6.3	0.4	0.8	[19]
Melting	573	374	–139	7.2	0.5	0.8	[30]
Melting	600	250	–167	7	0.52	0.8	[15]
Melting	550	222	–168	6.3	0.37	0.95	[17]
Melting	623	211.8	–177	6.6	0.43	0.97	[41]
Melting	350	679.8	–178	21.54	1.96	1.08	[42]

Table S3. EDS results of $Ag_2Te_{0.2}S_{0.8}$.

		#65	**#66**	**#67**	**#68**	**#69**
Ag_2S phase	Ag (at%)	68.87	67.14	67.40	66.72	68.73
	S (at%)	29.35	30.38	30.38	30.29	29.17
	Te (at%)	1.78	2.48	2.22	2.99	2.10

		#70	**#71**	**#72**	**#73**	**#74**
Ag_2Te phase	Ag (at%)	68.62	68.18	68.10	68.13	68.41
	Te (at%)	31.38	31.82	31.90	31.87	31.59

Reference

1. G. Kresse and J. Hafner, *Phys. Rev. B*, 1994, **49**, 14251-14269.
2. G. Kresse and J. Hafner, *Phys. Rev. B*, 1993, **47**, 558-561.
3. G. Kresse and J. Furthmüller, *Comp. Mater. Sci.*, 1996, **6**, 15-50.
4. G. Kresse and J. Hafner, *J. Phys. Condens. Mat.*, 1994, **6**, 8245-8257.
5. G. Kresse and J. Furthmüller, *Phys. Rev. B*, 1996, **54**, 11169-11186.
6. G. Kresse and D. Joubert, *Phys. Rev. B*, 1999, **59**, 1758-1775.
7. J. P. Perdew, K. Burke and M. Ernzerhof, *Phys. Rev. Lett.*, 1996, **77**, 3865-3868.
8. W. Setyawan and S. Curtarolo, *Comp. Mater. Sci.*, 2010, **49**, 299-312.
9. F. Tran and P. Blaha, *Phys. Rev. Lett.*, 2009, **102**, 226401.
10. T.-R. Wei, P. Qiu, K. Zhao, X. Shi and L. Chen, *Adv. Mater.*, 2023, **35**, 2110236.
11. X. Shi, A. Wu, T. Feng, K. Zheng, W. Liu, Q. Sun, M. Hong, S. T. Pantelides, Z. G. Chen and J. Zou, *Adv. Energy Mater.*, 2019, **9**, 1803242.
12. X. Shi, A. Wu, W. Liu, R. Moshwan, Y. Wang, Z.-G. Chen and J. Zou, *ACS Nano*, 2018, **12**, 11417-11425.
13. M. Jin, X.-L. Shi, T. Feng, W. Liu, H. Feng, S. T. Pantelides, J. Jiang, Y. Chen, Y. Du, J. Zou and Z.-G. Chen, *ACS Appl. Mater. Interfaces*, 2019, **11**, 8051-8059.
14. X. L. Shi, K. Zheng, M. Hong, W. D. Liu, R. Moshwan, Y. Wang, X.-L. Qu, Z. G. Chen and J. Zou, *Chem. Sci.*, 2018, **9**, 7376-7389.
15. S. Yang, Z. Gao, P. Qiu, J. Liang, T.-R. Wei, T. Deng, J. Xiao, X. Shi and L. Chen, *Adv. Mater.*, 2021, **33**, 2007681.
16. H. Wu, X.-L. Shi, Y. Mao, M. Li, W.-D. Liu, D.-Z. Wang, L.-C. Yin, M. Zhu, Y. Wang, J.

Duan, Q. Liu and Z.-G. Chen, *Adv. Energy Mater.*, 2023, **13**, 2302551.

17. Y. Wang, Q. Chen, P. Qiu, Z. Gao, S. Yang, L. Xi, J. Yang and X. Shi, *Adv. Funct. Mater.*, 2024, DOI: https://doi.org/10.1002/adfm.202415008, 2415008.

18. J. Liang, T. Wang, P. Qiu, S. Yang, C. Ming, H. Chen, Q. Song, K. Zhao, T.-R. Wei, D. Ren, Y.-Y. Sun, X. Shi, J. He and L. Chen, *Energy Environ. Sci.*, 2019, **12**, 2983-2990.

19. H. Chen, C. Shao, S. Huang, Z. Gao, H. Huang, Z. Pan, K. Zhao, P. Qiu, T.-R. Wei and X. Shi, *Adv. Energy Mater.*, 2024, **14**, 2303473.

20. S. He, Y. Li, L. Liu, Y. Jiang, J. Feng, W. Zhu, J. Zhang, Z. Dong, Y. Deng, J. Luo, W. Zhang and G. Chen, *Sci. Adv.*, 2020, **6**, eaaz8423.

21. Z. Li, J. Zhang, S. Wang, Z. Dong, C. Lin and J. Luo, *Scripta Mater.*, 2023, **228**, 115313.

22. H. Wang, X. Liu, B. Zhang, L. Huang, M. Yang, X. Zhang, H. Zhang, G. Wang, X. Zhou and G. Han, *Chem. Eng. J.*, 2020, **393**, 124763.

23. W. Zhou, W. Zhao, Z. Lu, J. Zhu, S. Fan, J. Ma, H. H. Hng and Q. Yan, *Nanoscale*, 2012, **4**, 3926-3931.

24. T. Zhu, X. Su, Q. Zhang and X. Tang, *J. Alloys Compd.*, 2021, **871**, 159507.

25. A. K. Gautam and N. Khare, *ACS Appl. Energy Mater.*, 2023, **6**, 6666-6672.

26. Y. Wang, P. Qiu, S. Yang, Z. Gao, L. Chen and X. Shi, *J. Materiomics*, 2024, **10**, 543-551.

27. L. Feng, A. Guo, K. Liu, H. Bai, J. Lv, Q. Zhang, J. Wu, X. Su, X. Tang and C. Uher, *Mater. Today Phys.*, 2023, **33**, 101051.

28. Y. Xu, M. Yan, E. Jiang, Z. Zheng, H. Wang, B. Duan, G. Li and P. Zhai, *Mater. Lett.*, 2023, **339**, 134100.

29. H. Hu, K. Xia, Y. Wang, C. Fu, T. Zhu and X. Zhao, *J. Mater. Sci. Technol.*, 2021, **91**, 241-

250.

30. H. Hu, Y. Wang, C. Fu, X. Zhao and T. Zhu, *The Innovation*, 2022, **3**, 100341.

31. V. Sharma, D. Sharma, R. Bhatt, P. K. Patro and G. S. Okram, *ACS Appl. Energy Mater.*, 2022, **5**, 13887-13894.

32. Y. Chang, J. Guo, Y.-Q. Tang, Y.-X. Zhang, J. Feng and Z.-H. Ge, *CrystEngComm*, 2019, **21**, 1718-1727.

33. A. K. Gautam and N. Khare, *J. Materiomics*, 2023, **9**, 310-317.

34. T. Zhu, H. Bai, J. Zhang, G. Tan, Y. Yan, W. Liu, X. Su, J. Wu, Q. Zhang and X. Tang, *ACS Appl. Mater. Interfaces*, 2020, **12**, 39425-39433.

35. L. Li, C. Peng, J. Chen, Z. Ma, Y. Chen, S. Li, J. Wang and C. Wang, *J. Alloys Compd.*, 2021, **886**, 161241.

36. J. Liang, P. Qiu, Y. Zhu, H. Huang, Z. Gao, Z. Zhang, X. Shi and L. Chen, *Research*, 2020, **2020**, 6591981.

37. H. Wu, X.-L. Shi, Y. Mao, M. Li, T. Wu, D.-Z. Wang, L.-C. Yin, M. Zhu, W.-D. Liu, L. Wang, Y. Wang, J. Duan, Q. Liu and Z.-G. Chen, *Adv. Sci.*, 2024, **11**, 2408374.

38. J. Liang, X. Zhang and C. Wan, *ACS Appl. Mater. Interfaces*, 2022, **14**, 52017-52024.

39. S. Zhong, H. Luo, K. Liu, S. Chen, Z. Yang, Y. Zhong, J. Wu, X. Su, P. F. P. Poudeu, Q. Zhang and X. Tang, *ACS Appl. Mater. Interfaces*, 2024, **16**, 36637-36648.

40. D. Xie, Y. Chang, T. Liu, Z. Li and J. Luo, *ACS Appl. Energy Mater.*, 2022, **5**, 8878-8884.

41. X. Liang and C. Chen, *Acta Mater.*, 2021, **218**, 117231.

42. S. Singh, K. Hirata, D. Byeon, T. Matsunaga, O. Muthusamy, S. Ghodke, M. Adachi, Y. Yamamoto, M. Matsunami and T. Takeuchi, *J. Electron. Mater.*, 2020, **49**, 2846-2854.